IOP Publishing New J. Phys. 26 (2024) 023056 https://doi.org/10.1088/1367-2630/ad2a81

New Journal of Physics
The open access journal at the forefront of physics

Deutsche Physikalische Gesellschaft DPG
IOP Institute of Physics

Published in partnership with: Deutsche Physikalische Gesellschaft and the Institute of Physics

OPEN ACCESS

RECEIVED
24 October 2023

REVISED
7 February 2024

ACCEPTED FOR PUBLICATION
19 February 2024

PUBLISHED
29 February 2024

PAPER

Competition between drift and topological transport of colloidal particles in twisted magnetic patterns

Nico C X Stuhlmüller[1], **Thomas M Fischer**[2] and **Daniel de las Heras**[1,3,*]

[1] Theoretische Physik II, Physikalisches Institut, Universität Bayreuth, D-95440 Bayreuth, Germany
[2] Experimatalphysik X, Physikalisches Institut, Universität Bayreuth, D-95440 Bayreuth, Germany
[3] https://danieldelasheras.com/
[*] Author to whom any correspondence should be addressed.

E-mail: delasheras.daniel@gmail.com

Keywords: topological transport, drift transport, twisted bilayers, magnetic colloids, Brownian dynamics simulations, commensuration

Supplementary material for this article is available online

Abstract

We simulate the motion of paramagnetic particles between two magnetic patterns with hexagonal symmetry that are twisted at a magic angle. The resulting Morié pattern develops flat channels in the magnetic potential along which colloidal particles can be transported via a drift force of magnitude larger than a critical value. Colloidal transport is also possible via modulation loops of a uniform external field with time varying orientation, in which case the transport is topologically protected. Drift and topological transport compete or cooperate giving rise to several transport modes. Cooperation makes it possible to move particles at drift forces weaker than the critical force. At supercritical drift forces the competition between the transport modes results e.g. in an increase of the average speed of the particles in integer steps and in the occurrence of subharmonic responses. We characterize the system with a dynamical phase diagram of the average particle speed as a function of the direction of the topological transport and the magnitude of the drift force.

1. Introduction

Interesting phenomenology often emerges as a result of a competition between two physical effects. We study here the competition between two different transport types (topological and drift) in an out-of-equilibrium colloidal system inspired in twisted graphene [1–9]. Bilayers of graphene twisted to a magic angle show new emergent phenomena including superconductivity, ferromagnetism, antiferromagnetism and correlated insulator properties [2, 6, 10–13]. Topology plays a major role in these states [9, 14].

In our colloidal system [15], the particle transport shares some similarities with electronic transport in twisted graphene. Paramagnetic colloidal particles are placed between twisted hexagonal magnetic patterns. Due to the negative interference between the magnetic fields of both patterns, flat channels develop in the total magnetic potential acting on the particles. The flat channels percolate the entire system for patterns twisted at magic angles, in which case a weak drift force is able to sustain macroscopic transport.

We have also extensively studied (with computer simulations and experimentally) the topologically protected transport of paramagnetic colloids above single periodic magnetic patterns [16–20]. There, the transport is driven by a uniform external magnetic field of varying orientation. The orientation changes performing closed curves (loops) in the space of all possible orientations that we call control space. There exist special loops that induce particle transport. That is, once the orientation returns to the initial one (after one loop) the particle has been transported by at least one unit cell of the magnetic pattern. The loops that induce transport share in common that they wind around specific orientations. The transport direction depends exclusively on the set of winding numbers around these orientations. The winding numbers constitute therefore a topological invariant that protects the motion.

In this work, we use computer simulations to first study the topological transport in hexagonal magnetic patterns twisted at a magic angle. Next, we add a drift force acting on the particles along the direction of the

flat channels and investigate the competition between drift and topological transport. We present a dynamical phase diagram of the system in the plane of direction of the topological transport and strength of the drift transport. Several transport modes arise. Some of them result from commensuration effects that involve the length of the flat channels, the period of the modulation loop, and the strength of the drift force. We also discuss briefly how the transport is affected by the occurrence of Brownian motion (finite temperature effects).

2. Setup

Paramagnetic colloids are placed between parallel magnetic bi-layers of hexagonal patterns that are shifted by half a unit-vector and twisted at a magic angle [15]. A sketch of the system is shown in figure 1(a). The colloidal particles (suspended in an inert solvent) are free to move in the middle plane located between the patterns which we refer to as action space. Experimentally, restricting the motion to a plane is possible using e.g. a polymer coating that acts as a spacer above which the particles sediment [18].

Single hexagonal patterns can be generated by the superposition of three waves with wave vectors $\boldsymbol{q}_i$, $i = 1, 2, 3$ given by

$$\boldsymbol{q}_i(\alpha) = \frac{4\pi}{\sqrt{3}a}\boldsymbol{R}^{-\alpha}\begin{pmatrix}-\sin(2\pi i/3)\\ \cos(2\pi i/3)\end{pmatrix}, \tag{1}$$

where a is the magnitude of a lattice vector and $\boldsymbol{R}^{\alpha}$ is a two dimensional rotation matrix by an angle α around the axis normal to the pattern. At elevation z larger than the magnitude of a lattice vector ($z > a$), the magnetic field of a single pattern is well approximated by [15, 18, 20]

$$\boldsymbol{H}_{\mathrm{p}}(\boldsymbol{r};\alpha,\boldsymbol{r}_{\mathrm{s}}) = H_0 a\sum_{i=1}^{3}\begin{pmatrix}\boldsymbol{q}_i(\alpha)\sin(\boldsymbol{q}_i(\alpha)\cdot\boldsymbol{r}-\boldsymbol{R}^{\alpha}\boldsymbol{r}_{\mathrm{s}})\\ q\cos(\boldsymbol{q}_i(\alpha)\cdot\boldsymbol{r}-\boldsymbol{R}^{\alpha}\boldsymbol{r}_{\mathrm{s}})\end{pmatrix}, \tag{2}$$

where H_0 is the magnitude of the field of the pattern (controlled by the saturation magnetization of the pattern domains and the elevation z), $\boldsymbol{r}$ denotes the position in action space (i.e. a plane at constant elevation above the pattern), and $\boldsymbol{r}_{\mathrm{s}}$ is a shift vector (parallel to the pattern). The magnetic pattern that generates such magnetic field contains regions of positive and negative magnetization normal to the pattern, see figure 1(a), given by

$$\boldsymbol{M}(\boldsymbol{r};\alpha,\boldsymbol{r}_{\mathrm{s}}) = \boldsymbol{M}_0\mathrm{sign}\left(\sum_{i=1}^{3}\cos(\boldsymbol{q}_i(\alpha)\cdot\boldsymbol{r}-\boldsymbol{R}^{\alpha}\boldsymbol{r}_{\mathrm{s}})+1/2\right), \tag{3}$$

with $\boldsymbol{M}_0 = M_0\hat{\boldsymbol{e}}_z$ the saturation magnetization of the domains and $\hat{\boldsymbol{e}}_z$ the unit vector normal to the patterns. An external homogeneous magnetic field $\boldsymbol{H}_{\mathrm{ext}}$, much stronger in amplitude than $\boldsymbol{H}_{\mathrm{p}}$, drives the topological transport. The amplitude of the external field is constant in space and time, but its orientation varies with time performing loops. That is, after a loop is completed, the orientation returns to its initial value. The set of all possible orientations of $\boldsymbol{H}_{\mathrm{ext}}$ is the surface of a sphere which we refer to as control space $\mathcal{C}$, see figure 1(b).

The total magnetic potential, V, created by the twisted patterns and the external field is proportional to the scalar product of the total magnetic field with itself

$$V \propto -\left(\boldsymbol{H}_{\mathrm{p1}}+\boldsymbol{H}_{\mathrm{p2}}+\boldsymbol{H}_{\mathrm{ext}}\right)^2. \tag{4}$$

Here $\boldsymbol{H}_{\mathrm{p1}}$ and $\boldsymbol{H}_{\mathrm{p2}}$ are the magnetic fields of each of the twisted patterns. In the limit $|\boldsymbol{H}_{\mathrm{ext}}| \gg |\boldsymbol{H}_{\mathrm{p}}|$, the cross-term dominates the magnetic potential which simplifies them to [15]

$$V(\boldsymbol{r},t) = -2\chi\mu_0 v_{\mathrm{eff}}\left(\boldsymbol{H}_{\mathrm{p1}}(\boldsymbol{r})+\boldsymbol{H}_{\mathrm{p2}}(\boldsymbol{r})\right)\cdot\boldsymbol{H}_{\mathrm{ext}}(t). \tag{5}$$

Here t is the time variable, χ denotes the magnetic susceptibility of the particles, v_{eff} their effective volume, and μ_0 is the vacuum permeability.

The patterns are parallel to each other and shifted by half a unit-vector to maximize the negative interference of the magnetic fields along the flat channels. Then, we rotate the patterns by angles $\pm\alpha_{\mathrm{m}}/2$ around an axis normal to them, figure 1(a). We use here $\alpha_{\mathrm{m}}/2 = \arctan\left(\sqrt{3}/33\right) \approx 3.00°$ such that the total twist is α_{m}, which corresponds to the magic angle with the smallest drift force required to achieve macroscopic transport (when the external magnetic field is static and points normal to the patterns [15]).

Hence, using equation (2), the magnetic field of both patterns are then given by $\boldsymbol{H}_{\mathrm{p1}}(\boldsymbol{r}) = \boldsymbol{H}_{\mathrm{p}}(\boldsymbol{r};-\alpha_{\mathrm{m}}/2, \boldsymbol{a}_3/2)$ and $\boldsymbol{H}_{\mathrm{p2}}(\boldsymbol{r}) = \boldsymbol{H}_{\mathrm{p}}(\boldsymbol{r};\alpha_{\mathrm{m}}/2,\boldsymbol{0})$. The lattice vectors of the unrotated pattern are defined such that

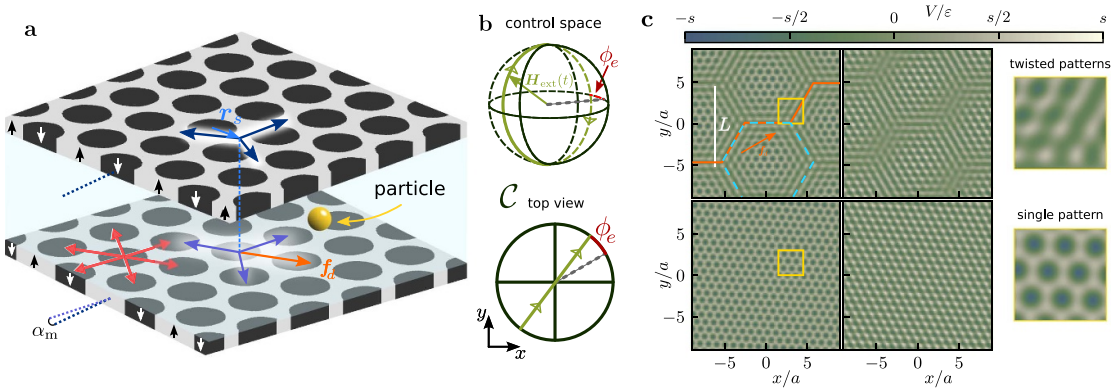

Figure 1. Setup and magnetic potential. (a) Schematic overview. A paramagnetic particle (yellow) is located in the middle plane between two parallel layers of thin magnetic hexagonal patterns shifted by an in plane vector $\boldsymbol{r}_s$ and afterwards rotated relative to each other by an angle α_m. Black and white regions are magnetized normal to the patterns but in opposite directions, as indicated by the white and black arrows. Violet (dark blue) arrows are three rotated lattice vectors of the bottom (top) pattern, i.e. $\boldsymbol{R}^{\pm\alpha_m/2}\boldsymbol{a}_i$. A drift force (orange arrow) pushes the particle in the direction of the zig-zag like flat channels. The red arrows in the bottom pattern indicate the topological transport directions in single patterns. (b) Control space $\mathcal{C}$ depicted by a wireframe sphere. Solid lines are reader facing while dashed lines indicate that they are on the back side of the sphere. The green circle is a modulation loop performed by $\boldsymbol{H}_{\text{ext}}(t)$, which is itself depicted at a particular orientation using a green arrow. The direction of the loop is characterized by the angle ϕ_e, shown in red. (c) Magnetic potential V (colorbar) for different orientations of the external magnetic field (left column: north, i.e. along the z-axis, center column: along the x-axis). The first row shows the potential in presence of both patterns. A zig-zag flat channel is highlighted in orange. A supercell is highlighted in blue. Note that it is also possible to choose the supercell differently such that the flat channels are not at the edges. The drift force points in the direction of the orange arrow. The second row is the potential when only the bottom pattern is present. The third column is a close view of selected regions (yellow squares). The scale bar is $s = 45$ (top row), and $s = 25$ (bottom row).

$\boldsymbol{a}_i \cdot \boldsymbol{q}_j(0) = \delta_{ij}$ for $i,j = 1,2$ and $\boldsymbol{a}_3 \cdot \boldsymbol{q}_3(0) = 0$. (the vector $\boldsymbol{a}_3$ is a linear combination of $\boldsymbol{a}_1$ and $\boldsymbol{a}_2$). The magnetic potential, equation (5), that results after insertion of the expressions for $\boldsymbol{H}_{\text{p1}}$ and $\boldsymbol{H}_{\text{p2}}$ using equation (2) is valid only at the middle plane between the patterns where the colloidal particles move.

Due to the interference between the fields of both patterns a Moiré pattern develops. We call the large periodic structures of the Moiré pattern supercells. These supercells have a supercell lattice constant of $L/a = 1/(2\sin(\alpha_{\text{m}}/2)) \approx 9.5$ [15]. Near the edges of the supercells there exist flat channels along which the magnetic potential is rather flat, see figure 1(c). The flat channels are the result of the negative interference of two wave vectors of the patterns, one from each pattern. Along the flat channels it is possible to transport colloidal particles using a weak external drift force. What makes magic angles special is that the resulting Morié pattern is periodic with a period of one supercell (smallest possible period).

Simulations. Experiments in closely related systems are in the overdamped regime [18]. We therefore use Brownian dynamics simulations to simulate the particle motion. Three different types of transport are involved: Brownian motion induced by the implicit solvent, drift transport originated by an external force constant in space and time, and topological transport facilitated through loops of the orientation of the external magnetic field. The equation of motion of a single particle is then

$$\gamma \dot{\boldsymbol{r}}_{\text{p}} = -\nabla V(\boldsymbol{r}_{\text{p}}, t) + \boldsymbol{f}_{\text{d}} + \boldsymbol{\eta}, \tag{6}$$

where $\boldsymbol{r}_{\text{p}}$ is the position of the particle, the overdot indicates time derivative, ∇ indicates the derivative with respect to $\boldsymbol{r}_{\text{p}}$, $\boldsymbol{\eta}$ is a delta correlated random force due to the implicit solvent, $\boldsymbol{f}_{\text{d}}$ is the drift force, and γ is the friction coefficient against the implicit solvent.

We use adaptive Brownian dynamics [21] to integrate the equation of motion (the maximum relative tolerance is set to 10^{-3} and the maximum absolute tolerance to $10^{-4}a$). We work in units of the lattice constant of the single patterns a, the friction coefficient γ, and the energy scale of the magnetic potential, defined as as $\epsilon = \chi\mu_0 v_{\text{eff}} H_0 H_{\text{ext}}$ which contains the relevant natural constants and particle characteristics together with the magnitudes of the magnetic fields, see equation (5). Note that the magnetic potential varies approximately $10^2\epsilon$ from minima to maxima in twisted patterns, see figure 1(c). Our time scale is given by $\tau = \gamma a^2/\epsilon$.

Most simulations are done at zero temperature (i.e. no Brownian motion) because in the experimental setups the Brownian motion is usually negligible as compared to the magnetic forces [19]. Nevertheless, we briefly analyze the effect of finite temperature on the transport at the end of the Results section.

3. Results

3.1. Pure topological transport

We first focus on the pure topological transport in twisted patterns. That is, the transport induced by modulation loops of the external magnetic field in absence of drift forces.

Topological transport in single patterns. The topological transport facilitated via magnetic forces above single periodic patterns [18–20] as well as inhomogeneous patterns [16, 17, 22] is well understood. Here, we briefly recap the fundamentals of the topological transport above periodic magnetic patterns.

The combination of the two magnetic fields (pattern and external) creates an intricate energy landscape not constant in space. See the bottom panels of figure 1(c) for the potential in hexagonal patterns corresponding to two orientations of the external field. To understand the transport of the colloidal particles we need to focus on the stationary points of the potential. The particles are adiabatically transported via a minimum of the potential (and travel to a minimum nearby via a ratchet in case that the transporting minimum disappears during the modulation loop). Note that a maximum can be always transformed into a minimum by simply inverting the orientation of the external magnetic field, see equation (5). The potential also contains saddle points but the particles can only rest in the minima of the potential since a saddle point is not a local equilibrium position. There exist regions above the pattern in which V can never be a minimum for any orientation of $\boldsymbol{H}_{\text{ext}}$. Those regions are called the forbidden regions [19] and they can contain only saddle points. The regions for which there exist an orientation in $\boldsymbol{H}_{\text{ext}}$ such that V is minimum are called the allowed regions. In the allowed regions it is always possible to find a minimum (or a maximum) of V but never a saddle-point. The complete action space splits into forbidden and allowed regions, the shape of which varies with the symmetry of the pattern [18].

The boundaries between allowed and forbidden regions in action space are the fences. The intersection of fences in action space are the gates as they allow particles to move from one allowed region to the adjacent one. Both fences and gates also exist in control space. To transport a particle in action space, the modulation loop in control space needs to wind around special orientations of the external field (called bifurcation points and determined by the position of the fences in $\mathcal{C}$ [18]). The set of winding numbers of the modulation loop around the bifurcation points in $\mathcal{C}$ is the topological invariant that protects the motion and determines the transport direction. The exact path followed by the loop in $\mathcal{C}$ is irrelevant in the sense that any two loops with the same topological invariant will transport a particle between the same type of allowed regions. In hexagonal patterns, it is possible to transport the particles along the six directions given by the lattice vectors, see red arrows in figure 1(a), which for an unrotated pattern are simply $\pm\boldsymbol{a}_i$ with $i = 1, 2, 3$.

Topological transport in twisted patterns. We investigate next the topological transport in hexagonal magnetic patterns twisted at a magic angle. To transport the particles, we impose an external magnetic field that orbits control space following great circles. The modulation loop crosses both poles of $\mathcal{C}$ and the equator at latitudes ϕ_{e} and $\phi_{\text{e}} + \pi$. We measure ϕ_{e} relative to the average direction between two consecutive flat channels (counterclockwise rotation by thirty degrees of the x-axis [15]). An illustration of a modulation loop together with $\mathcal{C}$ can be seen in figure 1(b). The period of one loop is set to $\tau_0/\tau = 5$. The total magnetic potential varies along the modulation loop. Figure 1(c) depicts the magnetic potential for two different orientations of the external magnetic field in both twisted and single patterns.

When continuously varying ϕ_{e} along the equator, the direction of transport locks into one of sixteen discrete directions, see particle trajectories in figure 2(a). Six of these directions point along the flat channels that develop near the edges of the supercells. Six other directions point along the lattice vectors of the hexagonal Morié grid. The last four directions point roughly orthogonal to the conducting flat channel. The topological transport between twisted pattern is possible along more directions than one would naively expect from the combination of two single patterns (i.e. $2 \times 6 = 12$ directions). Analogous to single patterns, the transport direction is not a continuous function of the orientation of the loop in control space, but it rather shows discrete topological transitions.

In order to measure the efficiency of the topological transport, we calculate the average speed of the particles during the modulation loop. We average over one hundred different realizations. The particles are initialized randomly in a square region with side length $10\,a$ around the origin that covers a complete supercell. To eliminate the dependence on the initial conditions, we let the system reach a steady state by applying fifty modulation loops before measuring the average speed μ during another fifty loops, i.e.

$$\mu = \frac{1}{50\tau_0} \left\langle \left| \boldsymbol{r}_{\text{p}}\left(100\,\tau_0\right) - \boldsymbol{r}_{\text{p}}\left(50\,\tau_0\right) \right| \right\rangle , \tag{7}$$

where $\langle\cdot\rangle$ denotes the average over the different realizations.

The average speed as a function of the angle ϕ_{e} is depicted in figure 2(b) for two values of the temperature $k_{\text{B}}T/\epsilon = 0$ and 0.1, with k_{B} the Boltzmann constant. The transport along any of the flat channels is faster

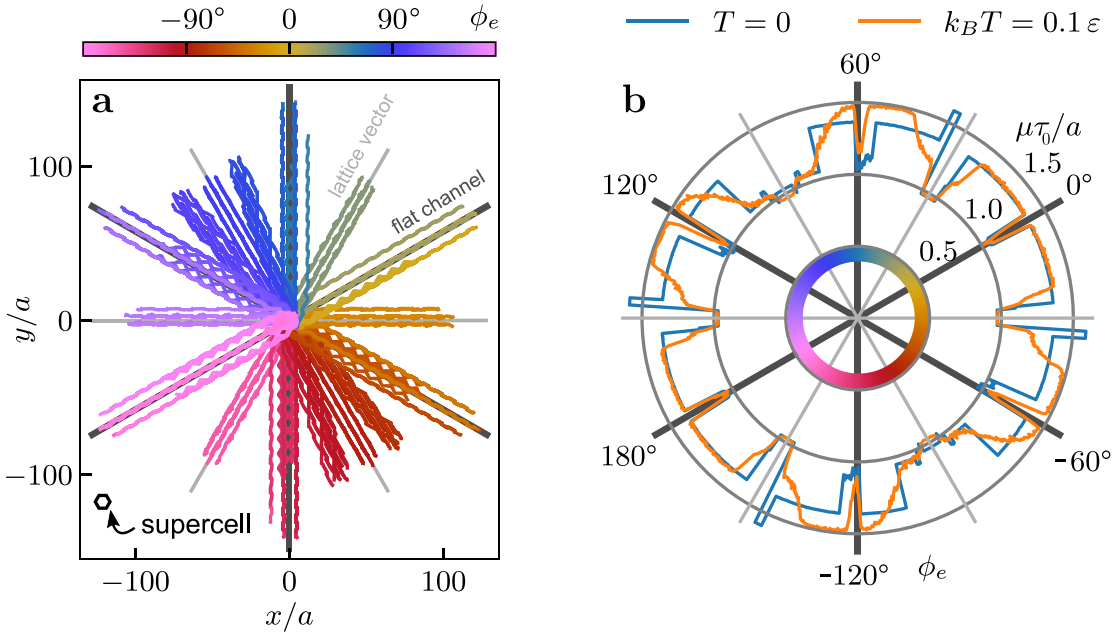

Figure 2. Pure topological transport. (a) Trajectories of particles located between patterns twisted at a magic angle. The small hexagon in the bottom left of (a) depicts the size of a supercell. The particles are randomly initialized around the origin and driven by 100 modulation loops of different orientation ϕ_e. The trajectories are colored according to the direction of the modulation loop ϕ_e (see color bar). (b) Average speed of the particles $\mu\tau_0/a$ for different values of the orientation of the modulation loops ϕ_e and two values of the temperature: $T = 0$ (blue line) and $k_BT/\epsilon = 0.1$ (orange line). Thick-dark gray lines point in the average direction of two consecutive flat channels. Thin-light gray lines point in the direction of the unit vectors of the supercells.

than that along the six directions of the underlying hexagonal patterns. In most cases, the particles that move along the flat channels do so with an average speed of approx. $1.4\,a/\tau_0$ and reach a peak speed of $1.6\,a/\tau_0$ in some specific cases. Note that slow topological transport (average speed $1\,a/\tau_0$) also occurs in narrow regions for values of ϕ_e close to the flat channel directions. This is likely due to the modulation loop crossing bifurcation points in the control space of the twisted patterns and causing the particles to intermittently deviate from the flat channel directions. In contrast, the average speed along the symmetry directions of the inner cells of the combined patterns is $1\,a/\tau_0$, which is the same as in single hexagonal patterns (one unit cell per loop). The overall increased speed along the flat channels arises from the Moiré pattern. Units cells with parallelogram symmetry and larger than the hexagonal cells form along the flat channels due to the negative interference between two pattern waves. Therefore, the particles travel a larger distance per loop along the flat channels than along the hexagonal lattice vectors (even though in both cases one modulation loop transports the particles one unit cell). The Brownian motion smooths, as expected, the zero temperature results but the main characteristics of the transport remain unchanged, cf the blue and orange curves in figure 2(b).

Concentrating particles into the flat channels. As discussed, there exist loops that transport the particles in the directions of the flat channels and hence it is possible to concentrate all particles in there. This is helpful for the transport in twisted patterns using drift forces [15] since the particles that are stuck inside the supercells could be moved towards the flat channels and become therefore mobile.

3.2. Pure drift transport

Before we discuss the interplay between drift and topological transport, we briefly summarize the transport due to only drift forces. A complete description of the pure drift transport is given in [15]. There, the external magnetic field is static and points normal to the pattern. A uniform drift force of magnitude f_d drives the motion. The optimal direction of the drift force is along the average direction of two consecutive flat channels, see figure 1(c). For patterns twisted at magic angles, the magnetic potential is periodic with a periodicity of one supercell. The particles can get pushed easily through the flat channels located near the edges of supercells provided that the magnitude of the drift force is above a critical value f_c. For the system investigated here the critical force is $f_c = 39.5\,\epsilon/a$ [15]. For weaker drift forces the particles located in a flat channel get stuck at the corners of the supercells, i.e. the place where two flat channels meet. The particles that are located outside of the flat channels are forever trapped even for magnitudes of the drift force much larger than the critical one.

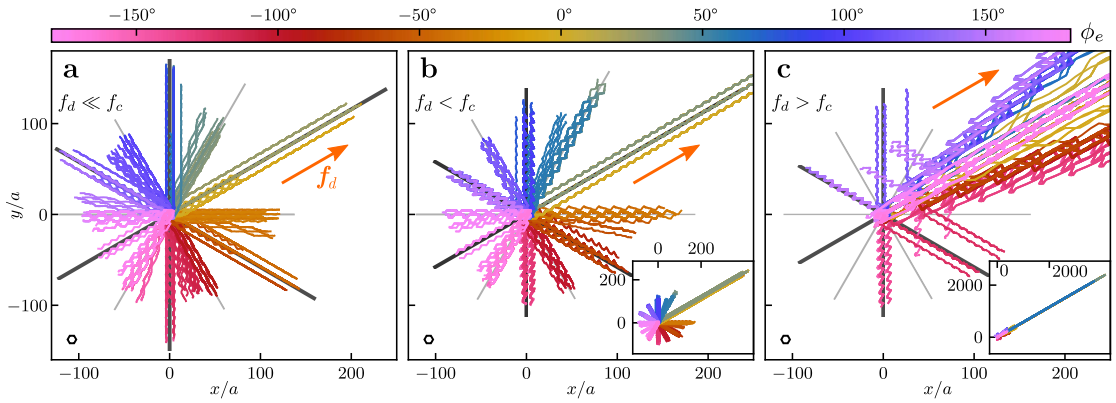

Figure 3. Topological and drift transport. Trajectories of particles located between patterns twisted at a magic angle and driven by both a drift force of magnitude f_d and 100 modulation loops of orientation ϕ_e. The particles are randomly initialized around the origin. The trajectories are colored according to the direction of the modulation loop ϕ_e (see color bar). The magnitude of the drift force is $f_d a/\epsilon = 5$ (a), 25 (b), and 45 (c). That is, below (a), (b) and above (c) the critical drift force $f_c a/\epsilon = 39.5$. The insets in panels (b) and (c) show the complete trajectories of the particles after 100 loops. The orange arrows indicate the direction of the drift force.

3.3. Combined drift and topological transport

In figure 3 we show the trajectories of particles subject to both a drift force and a modulation loop of the external magnetic field. The trajectories are colored according to the orientation of the modulation loop ϕ_e. We depict trajectories for a drift force much weaker, weaker, and stronger than the critical drift force in figures 3(a)–(c), respectively. Even at subcritical drift forces the speed in the direction of the drift force is increased. For weak drift forces, $f_d \ll f_c$, the particles are pushed along the flat channels until they hit a corner and get stuck. Therefore the particles can travel up to a distance L per loop even if $f_d \ll f_c$.

At supercritical drift forces, $f_d > f_c$, the particles can overcome the potential barriers at the corners of the supercells and the transport is then dominated by the drift force. At first glance, the topological transport hinders the transport along the flat channels as compared to a system without topological loops. There, $\boldsymbol{H}_{ext}$ always points normal to the patterns which is optimal to increase the colloidal mobility. However, to achieve macroscopic transport the topological loops are important. Without the modulation loops, only the particles that are initialized close enough to a flat channels can move. Particles inside the supercells would remain there. The topological loops are able to move the particles towards the flat channels and therefore to enable macroscopic transport.

A general effect of the drift force is that the direction of transport migrates towards the average direction between two consecutive flat channels. This is expected since whenever a particle enters a flat channel, it gets transported along the channel.

3.4. Dynamical phase diagram

To rationalize the complex interplay between drift and topological transport, we plot in figure 4(a) a dynamical phase diagram in which we represent the average speed μ (color coded), see equation (7), as a function of the direction of the topological loop (ϕ_e) and the magnitude of the drift force (f_d). The competition between the drift force and the topological transport generates a rich phenomenology. Two main regions corresponding to sub- and super-critical drift forces are clearly visible, see figures 4(b) and (c), respectively. We have identified several transport modes for which we show illustrative trajectories in figure 4 panels (d)–(l) and in the supplementary movies.

3.5. Sub-critical drift forces

We discuss first the region where the amplitude of the drift force is below the critical value that would allow particles to move freely through the flat channels [15], i.e. $f_d < f_c$.

Enhanced transport. Even for very weak drift forces, the particles can traverse the flat channels near the edges of supercells when the external magnetic field points normal to the pattern. However, they can not overcome the potential barrier that exists in the corners of the flat channels as long as the amplitude of the drift force is subcritical. Topological transport induced by a nontrivial loop is needed in order to move the particles around the corner and hence achieve macroscopic transport. There are two corners that need to be crossed per supercell. Hence, the highest average speed that we would naively expect is $\mu \approx L/(2\tau_0) \approx 4.77\, a/\tau_0$. This value corresponds to particles crossing one corner per modulation loop.

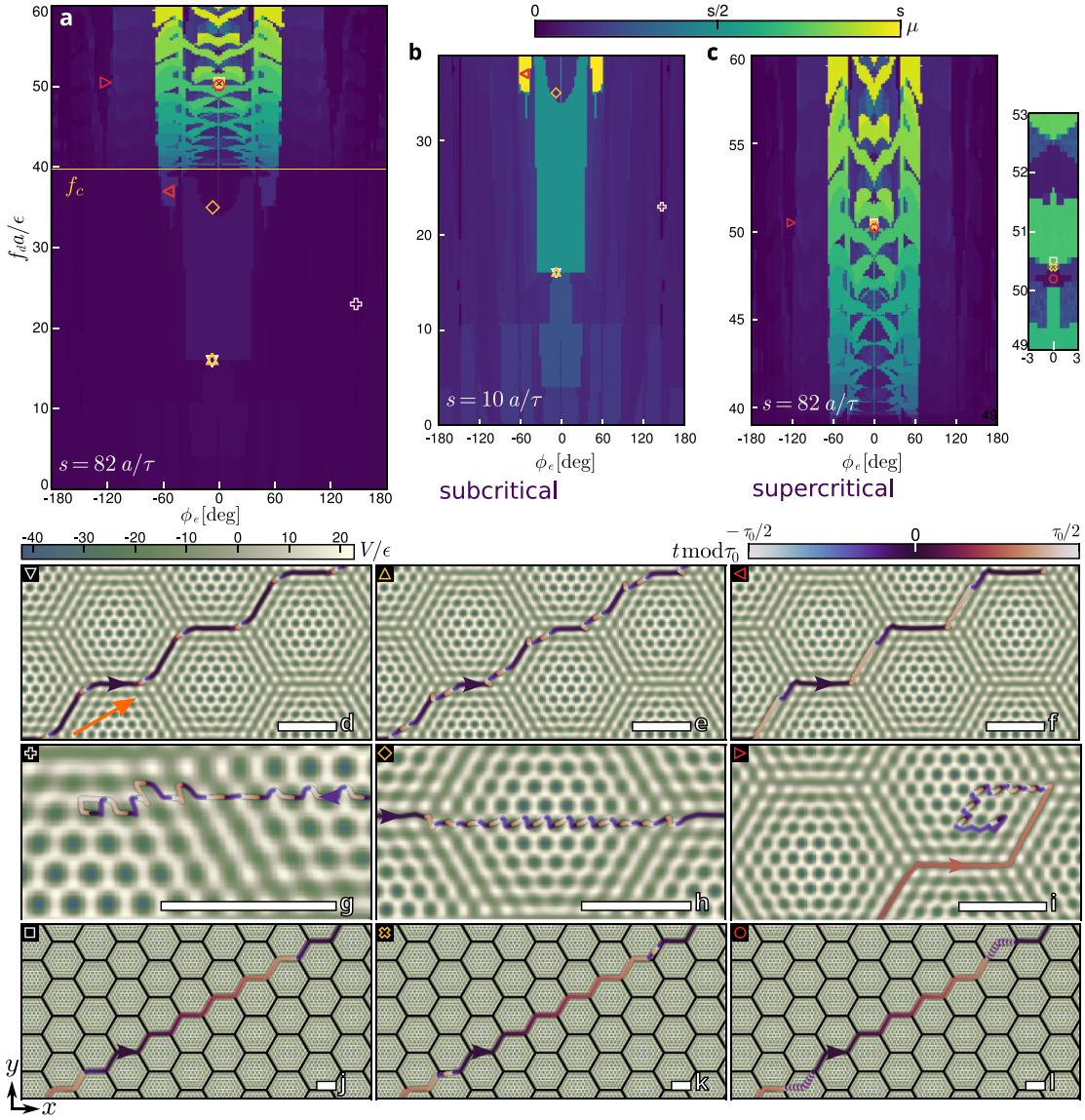

Figure 4. Dynamical phase diagram. Average speed of the particles (μ colorbar) as a function of the direction of the modulation loops ϕ_e and the amplitude of the drift force f_d. Panel (a) shows the complete dynamical phase diagram, whereas panels (b) and (c) are enlarged views of the subcritical $f_\mathrm{d} < f_\mathrm{c}$ and supercritical regions $f_\mathrm{d} > f_\mathrm{c}$. The yellow line in (a) indicates the critical drift force. The resolution in panels (a), (b), and (c) is $0.1\,a/\epsilon$ and 3° for the main panels and 0.3° for the close view in (c). Illustrative trajectories at specific state points (indicated by symbols) are shown in panels (d)–(l). The background depicts the magnetic potential (V colorbar) when the external magnetic field points along the z-axis (north of control space). The orange arrow in (d) indicates the direction of the drift force. The particle trajectories are colored according to the temporal evolution of the external loops that drives them ($t \mod \tau_0$ colorbar). The loop points towards the north (south) of control space if $t \mod \tau_0$ is in an interval of width $\tau_0/4$ around 0 ($\tau_0/2$). In panels (j) to (l) the supercells are surrounded by a black outline to increase their visibility. The scale bars have a length of $5a$. The amplitudes of the drift forces are $f_\mathrm{d} a/\epsilon = 16.1$ (d), 16.0 (e), 37.0 (f), 23.0 (g), 35.0 (h), 50.5 (i), 50.5 (j), 50.4 (k), 50.2 (l) and the orientation of the modulation loop $\phi_e = -7.5^\circ$ (d), -7.5° (e), -52.5° (f), 147.0° (g), -7.5° (h),-172.5° (i), 0.0° (j), 0.0° (k), 0.0° (i).

Depending on the value of ϕ_e, the modulation loop can transport the particles into a conducting flat channel, into a nonconducting channel, or into the inner regions of supercells. To achieve high speed transport at subcritical drift forces, we need to transport particles from one conducting channel to the next one using the least possible amount of loops. This can be done with only a single loop provided that ϕ_e is within the approximate interval $[-40^\circ, 40^\circ]$ and that $f_\mathrm{d} > 16\,\epsilon/a$. In this case, an average speed of $\mu \approx L/(2\tau_0) \approx 4.77\,a/\tau_0$ can be reached, see figures 4(a) and (b). Illustrative trajectories showing this transport mode are shown in figure 4(d) and supplementary movie 1.

A transport mode with half the average speed of the previous mode is shown in figure 4(e) and supplementary movie 2. This mode happens for smaller drift forces, i.e. $f_\mathrm{d} < 16\,\epsilon/a$, but within roughly the same interval of orientations of the external loop, see figure 4(b). Here the drift force is not strong enough to push the particles into the corner of the flat channels. Instead, the particles stop approximately one unit cell away from the corner. Therefore, two modulation loops are required for the particles to cross each corner.

One loop is needed to transport the particle into the corner and another loop to transport the particle over the corner. This results in an average speed of half a flat channel per loop, i.e. $\mu \approx L/(4\tau_0) \approx 2.38$.

If the particles get scattered into non-conducting channels or into a supercell, the average speed becomes close to $\mu \sim a/\tau_0$, as it takes of the order of L/a loops to traverse the supercell and hence get back to a conducting channel. This transport mode is also present at supercritical drift forces. An illustrative trajectory is shown in figure 4(h) and supplementary movie 3.

Unexpectedly, an average speed corresponding to traverse one entire supercell per loop is also possible even for subcritical drift forces. This transport mode is due to the occurrence of secondary transient flat channels parallel to the main flat channel and separated by a distance of half the magnitude of a lattice vector [15]. These flat channels become the local minimum when the external magnetic field points towards the south pole of $\mathcal{C}$. For a range of drift forces and orientations of the modulation loop, there exist a commensuration effect between the drift and the topological transport. The external field switches from north to south and back to north at the right times when the particles are sufficiently close to the corners of the supercells. This allows the particles to pass the corner by moving to the active flat channels at all times during the loop. As a result the particles are never stuck in the corners and travel always in a flat channel with average speed of $\mu \approx L/\tau_0 \approx 9.57\, a/\tau_0$. A trajectory is shown in figure 4(f) and supplementary movie 4. Note how the loop moves the particles from one channel to the next one at positions close to the corners of the supercells.

Reduced transport. The interplay between topological and drift transport can also reduce the average speed below that of the pure topological transport $\mu \approx a/\tau_0$. For external loops with directions ϕ_e within the intervals $[-180°, -90°]$ and $[90°, 180°]$ an average speed of less than one unit cell per loop is prevalent. In this region, the modulation loops transport the particles in a direction with a component opposite to the drift force. When the particles enter a flat channel they move along the channel, i.e. opposite to the direction facilitated by the modulation loops. As a result the average speed decreases substantially. In extreme cases, the average speed vanishes as the particles get trapped in a closed trajectory where the modulation loop and the drift force cause particles to never leave an area of one unit cell. An illustrative particle trajectory is shown in figure 4(g) and supplementary movie 5.

3.6. Supercritical drift forces

At drift forces larger than the critical drift force, i.e. $f_\mathrm{d} > f_\mathrm{c}$, the dynamical phase diagram shows a complex structure for modulation loops pointing roughly in the interval $\phi_\mathrm{e} \in [-60°, 60°]$, see figures 4(a) and (c). Here, regions of high and low average speed alternate quickly when increasing the magnitude of the drift force. Fast transport is achieved when the particles stay in the flat channels, see an example in figure 4(j) and supplementary movie 6. In these cases the particles can get trapped at the corners of the supercells when the loop blocks the corner. The loop then continues in such a way that the particles are transported through the corner into the flat channel. Recall that the critical drift force corresponds to the optimal orientation of the external field (pointing towards the north of control space). Hence, even though we explore now the region $f_\mathrm{d} > f_\mathrm{c}$ the particles can get stuck at the corners for other orientations of the external field.

In the slow regions, the particles are forced to move inside the supercells by the topological transport. There they need of the order of L/a loops to traverse the supercell and reach a flat channel again. Once they are in a flat channel they can traverse it during one loop, after which they are forced back into the interior region of a supercell. Averaging over many loops causes the average speed of the particles to be of order a/τ_0 since the low speed in the supercells dominates over the high speed in the flat channel. An illustrative trajectory is shown in figure 4(l) and supplementary movie 7.

When going from one region of high speed to the next one by increasing the drift force, see figure 4(c), the average speed increases by the length of one edge of a supercell per loop, i.e. $L/(2\tau_0)$. Due to the stronger drift force, the particles can travel along the flat channels at higher speed which allows them to traverse one more edge during the loop as compared to the previous high speed region.

The shape of the fast regions in the dynamical phase diagram resembles the Hofstadter's butterfly [23], known from the commensuration effects in the quantum Hall effect and in twisted bilayer graphene [24, 25]. Here, commensuration effects between the topological and the drift transport occur. The time required to traverse one edge of a supercell is roughly $t_\mathrm{e} \approx (L/2)/\mu_\mathrm{e}$ with μ_e the speed along the flat channel. At zero temperature, μ_e is mostly determined by the drift force $\mu_\mathrm{e} \approx f_\mathrm{d}/\gamma$, and hence $t_e \approx \gamma(L/2)/f_\mathrm{d}$. When the period of the modulation loop commensurates with this time there is fast region in the supercritical dynamical phase diagram. Since in our system $L/a \approx 9.5$ and $\tau_0 = 5\tau$ we expect fast regions to occur at intervals $\Delta f_\mathrm{d} \approx 1$ which is consistent with the simulation results, figure 4(c). If t_e and τ_0 do not commensurate, the particles get transported in the interior regions of the supercells and their average speed is reduced considerably.

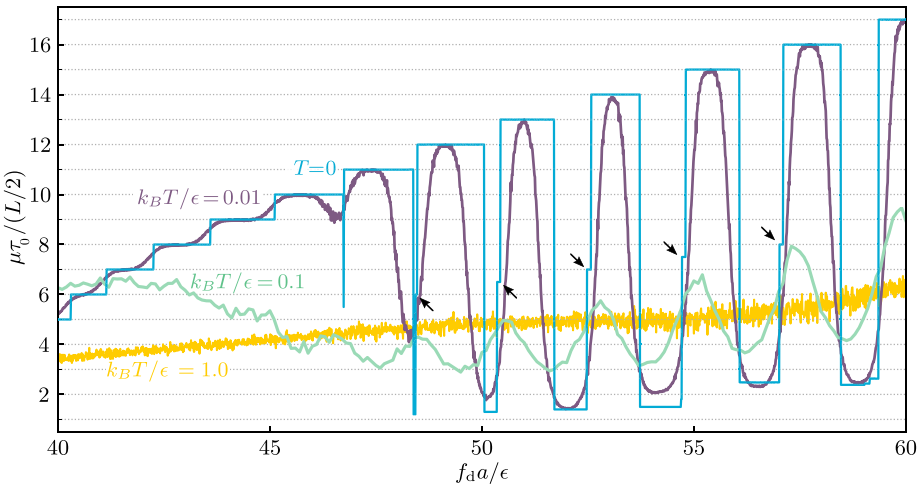

Figure 5. Scaled average speed. Average speed μ (scaled with the speed corresponding to travel half a supercell per loop) as a function of the magnitude of the drift force f_d in the supercritical region ($f_d > f_c$). The direction of the modulation loop is $\phi_e = 0$. The arrows indicate the regions in which at zero temperature (blue curve) the average speed jumps to half the value of the next high average speed region. The horizontal dotted-lines indicate the integer values of the scaled average speed. Results for several values of the temperature are shown: $T = 0$ (blue), $k_BT/\epsilon = 0.01$ (violet), $k_BT/\epsilon = 0.1$ (green), and $k_BT/\epsilon = 1.0$ (yellow).

If one rescales the average speed of the particles by the length of flat channels, i.e. measure the average speed in units of $L/(2\tau_0)$, the rescaled average speed increases (at zero temperature) in integer steps, similar to the quantum Hall effect, see figure 5. The figure corresponds to a vertical cut of the dynamical phase diagram for supercritical drift forces and $\phi_e = 0°$. A close inspection to the data shown in the figure reveals that there exists an intermediate step between fast and slow regions in which the response is subharmonic. There, the particles never leave the flat channels but they require two loops to continue their path along the flat channel. This phenomenon can be seen in figure 4(k) and supplementary movie 8. The system responds with only half the frequency of the external modulation.

Complete stop. Even for supercritical drift forces, there are large regions of the phase diagram with very low average speed. There, the direction of the topological transport opposes the direction of the drift force. In some cases the particles can be brought to a complete halt. See an illustrative trajectory in figure 4(i) and supplementary movie 9. This happens for supercritical forces and loop orientations ϕ_e within the intervals $[-180°, -155°]$ and $[155°, 180°]$ approximately.

3.7. Finite temperature

The general structure of the phase diagram is robust against Brownian motion. We show in figure 6 the dynamical phase diagram at temperature $k_BT/\epsilon = 0.1$. The alternation between fast and slow regions for supercritical forces resembles those found in the limit of vanishing temperature, figure 4(a). The discrete steps in the average speed get broadened by raising the temperature and, depending on the temperature, the plateaus might not reach the same heights. This broadening is wider than the size in which the subharmonic response occurs, which therefore vanishes rapidly with rising temperature (compare the zero and finite temperature curves in figure 5). Other complex transport modes are also rather sensitive to a temperature increase. For example, the mode shown in figure 4(f), which occurs at subcritical drift forces, requires a delicate commensuration effect between drift and topological transport. At relatively low temperatures ($k_BT/\epsilon \gtrsim 0.01$) the particle trajectories start to deviate from the zero temperature limit. Nevertheless, the main features of the dynamical phase diagram at subcritical forces remain the same in presence of Brownian motion. Particles can reach an average speed of more than one supercell per loop even for drift forces smaller than the critical force. This was expected as thermal fluctuations allow the particles to cross the corners of flat channels even if the drift force is not strong enough.

At sufficiently high temperatures ($k_BT/\epsilon \sim 1$), the Brownian motion becomes dominant, and the complex structure of the dynamical phase diagram disappears (see e.g. the high temperature curve in figure 5).

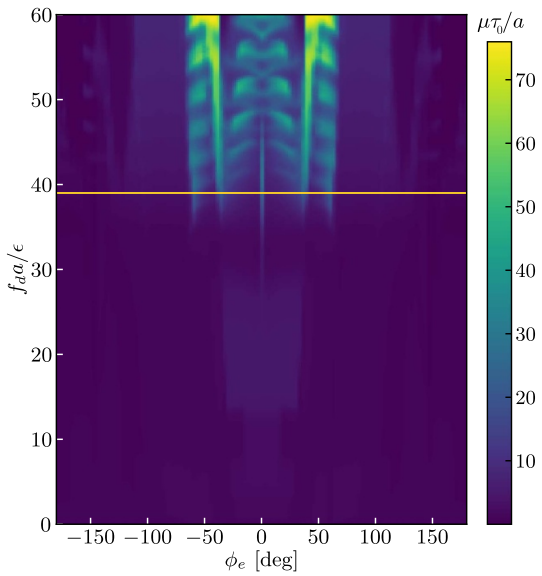

Figure 6. Finite temperature. Dynamical phase diagram at finite temperature ($k_B T/\epsilon = 0.1$) of the average speed of the colloidal particles μ (colorbar) in the plane of direction of the topological loop ϕ_e and magnitude of the drift force f_d. The horizontal yellow line indicates the magnitude of the critical drift force in the limit of zero temperature.

4. Conclusions

We have shown that topologically nontrivial loops of the orientation of a uniform external magnetic field can transport paramagnetic particles located between twisted magnetic patterns. Topological transport is possible along several directions including the flat channels of the twisted Moiré pattern and the lattice vectors of the hexagonal pattern that emerges inside the supercells.

The competition between topological and drift transport gives rise to a plethora of interesting transport modes. These include integer steps in the average speed of the particles, a subharmonic response, and a complete transport stop.

Based on previous works [16–19], we expect a good agreement between simulations an experiments. It should however be noted that small imperfections on the magnetization domains can have a large effect on the transport along flat channels using only drift forces [26]. Hence, very precise magnetic patterns might be required to observe the complete phenomenology reported here. Performing experiments on twisted patterns is not as simple as using single patterns. Simply tracking the motion of particles sandwiched between two opaque patterns is already not simple since optical microscopy is no longer possible. As an alternative, one could create single magnetic patterns designed to mimic the pattern field of two patterns twisted at magic angles. Once the single pattern is created the twist angle cannot be modified. Hence, to study the effect of the twist angle several patterns need to be fabricated. Since the topological transport is quite robust we expect a qualitative agreement between experimental and simulation results but very precise patterns might be required to achieve quantitative agreement since small imperfections might impact the drift transport also in single patterns.

A gradient pressure and the gravitational field are examples of possible drift forces that could be used in e.g. a magnetophoretic device [27–29].

We have only considered the limit of very dilute suspensions with no interparticle interactions. It would be interesting to study the effects that the many-body interparticle interactions have on the transport. Many-body non-equilibrium superadiabatic forces [30, 31] might alter the dynamical phase diagram and new states such as the occurrence of solitons [32, 33] might appear. Interparticle repulsion might scatter particles away from the flat channels, while interparticle attraction could drag particles together through flat channels resulting in an increased mobility. Hydrodynamic effects, which have not been considered here, might also alter the phenomenology.

Data availability statement

The data cannot be made publicly available upon publication because they are not available in a format that is sufficiently accessible or reusable by other researchers. The data that support the findings of this study are available upon reasonable request from the authors.

Acknowledgments

We acknowledge funding by the Deutsche Forschungsgemeinschaft (DFG, German Research Foundation) under Project Number 531559581.

ORCID iDs

Nico C X Stuhlmüller https://orcid.org/0000-0003-0509-9559
Thomas M Fischer https://orcid.org/0000-0002-8852-6570
Daniel de las Heras https://orcid.org/0000-0003-3219-0518

References

[1] Saito Y, Yang F, Ge J, Liu X, Taniguchi T, Watanabe K, Li J, Berg E and Young A F 2021 Isospin Pomeranchuk effect in twisted bilayer graphene *Nature* **592** 220
[2] Nuckolls K P, Oh M, Wong D, Lian B, Watanabe K, Taniguchi T, Bernevig B A and Yazdani A 2020 Strongly correlated Chern insulators in magic-angle twisted bilayer graphene *Nature* **588** 610
[3] Shen C *et al* 2020 Correlated states in twisted double bilayer graphene *Nat. Phys.* **16** 520
[4] Kariyado T and Vishwanath A 2019 Flat band in twisted bilayer Bravais lattices *Phys. Rev. Res.* **1** 033076
[5] Hu G *et al* 2020 Topological polaritons and photonic magic angles in twisted α-MoO_3 bilayers *Nature* **582** 209
[6] Yankowitz M, Chen S, Polshyn H, Zhang Y, Watanabe K, Taniguchi T, Graf D, Young A F and Dean C R 2019 Tuning superconductivity in twisted bilayer graphene *Science* **363** 1059
[7] Bistritzer R and MacDonald A H 2011 Moiré bands in twisted double-layer graphene *Proc. Natl Acad. Sci.* **108** 12233
[8] Suárez Morell E, Correa J D, Vargas P, Pacheco M and Barticevic Z 2010 Flat bands in slightly twisted bilayer graphene: tight-binding calculations *Phys. Rev.* B **82** 121407
[9] Song Z, Wang Z, Shi W, Li G, Fang C and Bernevig B A 2019 All magic angles in twisted bilayer graphene are topological *Phys. Rev. Lett.* **123** 036401
[10] Sharpe A L, Fox E J, Barnard A W, Finney J, Watanabe K, Taniguchi T, Kastner M A and Goldhaber-Gordon D 2019 Emergent ferromagnetism near three-quarters filling in twisted bilayer graphene *Science* **365** 605
[11] Lu X *et al* 2019 Superconductors, orbital magnets and correlated states in magic-angle bilayer graphene *Nature* **574** 653
[12] Cao Y, Fatemi V, Fang S, Watanabe K, Taniguchi T, Kaxiras E and Jarillo-Herrero P 2018 Unconventional superconductivity in magic-angle graphene superlattices *Nature* **556** 43
[13] Cao Y *et al* 2018 Correlated insulator behaviour at half-filling in magic-angle graphene superlattices *Nature* **556** 80
[14] Po H C, Zou L, Senthil T and Vishwanath A 2019 Faithful tight-binding models and fragile topology of magic-angle bilayer graphene *Phys. Rev.* B **99** 195455
[15] Stuhlmüller N C X, Fischer T M and de las Heras D 2022 Enhanced colloidal transport in twisted magnetic patterns *Commun. Phys.* **5** 48
[16] Massana-Cid H *et al* 2019 Edge transport at the boundary between topologically equivalent lattices *Soft Matter* **15** 1539
[17] Loehr J *et al* 2018 Colloidal topological insulators *Commun. Phys.* **1** 4
[18] Loehr J *et al* 2017 Lattice symmetries and the topologically protected transport of colloidal particles *Soft Matter* **13** 5044
[19] Loehr J, Loenne M, Ernst A, de las Heras D and Fischer T M 2016 Topological protection of multiparticle dissipative transport *Nat. Commun.* **7** 11745
[20] de las Heras D, Loehr J, Loenne M and Fischer T M 2016 Topologically protected colloidal transport above a square magnetic lattice *New J. Phys.* **18** 105009
[21] Sammüller F and Schmidt M 2021 Adaptive brownian dynamics *J. Chem. Phys.* **155** 134107
[22] Stuhlmüller N C X, Farrokhzad F, Kuświk P, Stobiecki F, Urbaniak M, Akhundzada S, Ehresmann A, Fischer T M and de las Heras D 2023 Simultaneous and independent topological control of identical microparticles in non-periodic energy landscapes *Nat. Commun.* **14** 7517
[23] Hofstadter D R 1976 Energy levels and wave functions of bloch electrons in rational and irrational magnetic fields *Phys. Rev.* B **14** 2239
[24] Crosse J A, Nakatsuji N, Koshino M and Moon P 2020 Hofstadter butterfly and the quantum hall effect in twisted double bilayer graphene *Phys. Rev.* B **102** 035421
[25] Dean C R *et al* 2013 Hofstadter's butterfly and the fractal quantum hall effect in moiré superlattices *Nature* **497** 598
[26] Rossi A M E B, Ernst A, Dörfler M and Fischer T M 2024 Disorder scattering in classical flat channel transport of particles between twisted magnetic square patterns *Commun. Phys.* **7** 24
[27] Lim B, Reddy V, Hu X, Kim K, Jadhav M, Abedini-Nassab R, Noh Y-W, Lim Y T, Yellen B B and Kim C 2014 Magnetophoretic circuits for digital control of single particles and cells *Nat. Commun.* **5** 3846
[28] Chong W H, Leong S S and Lim J 2021 Design and operation of magnetophoretic systems at microscale: device and particle approaches *Electrophoresis* **42** 2303
[29] Abedini-Nassab R, Sadeghidelouei N and Shields C W 2023 Magnetophoretic circuits: a review of device designs and implementation for precise single-cell manipulation *Anal. Chim. Acta* **1272** 341425
[30] de las Heras D and Schmidt M 2020 Flow and structure in nonequilibrium brownian many-body systems *Phys. Rev. Lett.* **125** 018001
[31] de las Heras D, Zimmermann T, Sammüller F, Hermann S and Schmidt M 2023 Perspective: how to overcome dynamical density functional theory *J. Phys.: Condens. Matter* **35** 271501
[32] Antonov A P, Ryabov A and Maass P 2022 Solitons in overdamped brownian dynamics *Phys. Rev. Lett.* **129** 080601
[33] Cereceda-López E, Antonov A P, Ryabov A, Maass P and Tierno P 2023 Overcrowding induces fast colloidal solitons in a slowly rotating potential landscape *Nat. Commun.* **14** 6448